Electrocatalysis in confinement: metal-organic frameworks for oxygen reduction

Hoefnagel, M.E.

Chapter 3

Surveying the Homogeneity of a Molecular Electrocatalyst Embedded in a Metal-Organic Framework Using Operando Characterization

Homogeneous electrocatalysis generally yields low catalytic current densities due to the small number of catalytic centers at the electrode surface. Incorporating molecular catalysts in metal-organic frameworks (MOFs) has been proposed as a viable approach to immobilize these catalysts on electrodes and thereby increase current densities. In addition, molecular catalysts do not always remain in their homogeneous state, sometimes partially taking on a more heterogeneous character, which makes clear identification of the active species in homogeneous catalysis challenging. Despite the risk of losing homogeneity, most studies reported concerning molecular catalysts embedded in MOFs have so far overlooked possible formation of heterogeneous deposits during electrocatalysis. This chapter contains a more comprehensive study on the changes of homogeneity exhibited by a molecular catalyst embedded in a MOF. The Cu species that are formed in the NU1000|Cu-tmpaCOOH MOF before, during, and after the oxygen reduction reaction (ORR) are investigated using ex situ and operando X-ray absorption spectroscopy (XAS). The catalyst that initially displays a Cu^{2+} oxidation state forms Cu^{0} clusters upon application of a reductive potential. After electrolysis, these clusters undergo oxidation back to Cu^{2+}. These results reveal that despite an activity enhancement, Cu-based molecular catalysts embedded in MOFs lose their homogeneity during electrolysis. These findings emphasize the need to always account for possible changes in homogeneity of molecular catalysts regardless of supporting structures.

This Chapter has been published as an article: M.E. Hoefnagel, J.S.D. Rodriguez, S. Campos-Jara, O. Usoltsev, D.G.H. Hetterscheid, S. Louisia. *ChemSusChem*. **2025**, *xx,* e202501380.

3.1 Introduction

Due to their uniform distribution in a solution, homogeneous catalysts allow for more precise control over a given reaction compared to heterogeneous materials, which results in high selectivity and efficiency of a chemical reaction. Successful examples of homogeneous catalysis include Heck, Negishi and Suzuki coupling reactions, olefin metathesis, and enantioselective hydrogenation reactions.[1–5] Although it is relatively easy to gather mechanistic information, one should be aware that these homogeneous systems may degrade to clusters or nanoparticles under catalytic conditions, leading to ambiguity regarding the true active species.[6,7] Such problems particularly arise when harsh reaction conditions are applied in, for example, an electrochemical environment. Water-oxidation catalysts based on Fe, Ir, and Co were found to form FeOx, IrOx, and CoOx deposits, respectively.[8–10] Furthermore, Cu-based molecular catalysts are regularly found to form metallic Cu deposits, as shown in the case of the Cu(DAT) (DAT = 3,5-diamino-1,2,4-triazole) catalyst for the oxygen-reduction reaction (ORR).[11] Similarly, a Cu-phtalocyanine catalyst for the CO_2 reduction reaction (CO_2RR) was found to form Cu clusters in situ, which was associated with the observed selectivity towards methane.[12] Several techniques are being employed to study the homogeneity of a catalyst, that is, the extent to which it remains a molecular catalyst during the reaction.[7,13,14] For example, this can be evaluated electrochemically by measuring the cyclic voltammetry (CV) of an electrode used for catalysis with a homogeneous catalyst in a clean electrolyte solution. If the resulting CV exhibits redox features not belonging to the bare electrode itself, this activity originates from deposits on the electrode. Additionally, metal-ion scavengers can be used to bind metal ions that have dissociated from their ligands. Furthermore, homogeneity can be characterized by spectroscopic techniques, such as X-ray photoelectron spectroscopy (XPS),[15] UV-vis absorption spectroscopy,[16] mass spectrometry (MS),[17] nuclear magnetic resonance (NMR),[18] and X-ray absorption spectroscopy (XAS).[19]

Recent years show an increase in the number of reports describing homogeneous catalysts immobilized in metal organic frameworks (MOFs) as a strategy to improve their stability or immobilize them on an electrode thereby increasing current densities.[20,21] Additionally, the use of MOFs may allow for more control over reactivity through confinement of active sites, reactants, and products.[22–25] The possibility to infinitely vary the structure of the framework by alterations of the linkers and nodes makes them interesting materials to study first and second coordination-sphere effects on catalysis.[26–29]

Although immobilizing a homogeneous catalyst in a MOF presents in theory multiple advantages, few reports comment on the homogeneity of molecular catalysts immobilized in MOFs. However, this is of utmost importance given the tendency of many molecular electrocatalysts to form heterogeneous deposits. The effects of high local concentrations of catalysts, reactants and protons in a confined space are largely unexplored yet make these MOF-embedded systems potentially vastly different from their homogeneous equivalents. This is especially important to consider for Cu-based molecular catalysts because of the low energetic barriers and, therefore, fast kinetics in ligand-exchange reactions.[30] When Cu ions are pulled from the equilibrium by the accumulation of Cu or CuO_x particles, rapid decomposition of homogeneous Cu catalysts may occur. These equilibria may be highly dynamic and shift with the applied reaction conditions.[26] Well-performing molecular catalysts based on Cu have been developed for CO_2 reduction,[31,32] hydrogen evolution,[33,34] water oxidation,[35,36] and oxygen reduction reactions.[37,38] However, various reports have shown that the molecular Cu catalyst is not always the active species.[11,12,39] In the works of Fontecave[39] and Wang[12], Cu^0 clusters were observed under operando conditions that were not visible with ex-situ characterization. In both cases, a Cu^{2+} species was observed before and after the reaction, but Cu^0 species with distinguishable Cu-Cu distances were observed during CO_2 reduction. Fontecave and coworkers developed an N-doped carbon material with single atom Cu catalysts for CO_2RR and suggested that the metallic Cu clusters formed in situ are the true active species.[39,40] Similarly, Wang identified Cu clusters formed in situ from Cu-phtalocyanine as the active catalysts with a high selectivity to methane during CO_2RR. These cases highlight the dynamic nature of Cu-based catalysts and thus, the importance of operando characterization to monitor processes occurring during reactions. Dynamic effects are still expected to occur when a molecular catalyst is incorporated in a MOF. Yet, to the best of our knowledge, no XAS characterization of MOF-embedded molecular catalysts has been reported so far.

In Chapter 2 is described how the Cu-tmpaCOOH catalyst for ORR was embedded in the Zr-based NU1000 MOF, which largely improved the reusability and catalytic stability of the catalyst compared to its use in homogeneous solutions.[41] However, cyclic voltammetry experiments after catalytic reactions show the presence of a new redox couple. This suggests that a different active species may be formed in the MOF. However, the presence of Cu-tmpaCOOH was shown to be crucial to obtain any catalytic activity. Given the dynamic properties of Cu species, the in-situ formation of Cu clusters observed by other groups, and our previous findings on the NU1000|Cu-tmpaCOOH MOF, it is clear that operando

techniques are required to (1) identify the active species present during the reaction and (2) understand the structural change that leads to loss of homogeneity. In this chapter, homogeneity of a molecular catalyst embedded in a MOF is studied before, during, and after electrocatalysis using ex situ and operando XAS.

3.2 Results and Discussion

3.2.1 The operando X-ray absorption spectroscopy experiment

In X-ray absorption spectroscopy experiments X-ray photons are absorbed by a core electron of the material to be studied.[42] From the excitation of this core electron a photoelectron is ejected from the orbital and the vacant orbital is subsequently filled by an electron from a higher-energy orbital. This transition is coupled to the ejection of a fluorescent photon. The energy of the absorbed X-rays depends on the nature of the material and on which core electron you wish to excite. When a core K-shell (1s) electron is excited, the resulting absorption edge is the K-edge of the species. The shape of the absorption edge and of the features before and after the absorption edge are determined by the electronic structure of the material.

The X-ray absorption near edge structure (XANES) is the region of the spectrum before the absorption edge, at the absorption edge and immediately after it. XANES is sensitive to details of the electronic states near the Fermi level or the highest occupied molecular orbital (HOMO) and lowest unoccupied molecular orbital (LUMO) and therefore gives information about local symmetry and oxidation state of the species. Therefore, this part of a Cu K-edge spectrum may give information about the oxidation state of Cu before, during and after ORR catalysis.

The extended X-ray absorption fine structure (EXAFS) is the region of the spectrum up to a few thousand eV above the absorption edge. Because of the high density of available electronic states and the high energy of the photoelectron in this region, EXAFS is sensitive to spatial arrangements of nearest neighbors around the absorbing atom. The EXAFS-derived R, N and σ values represent the radial distance, coordination number, and the measure of disorder in neighboring atoms, respectively. EXAFS in k-space is a function of the photoelectron wavenumber k. The Fourier transform of EXAFS in k-space gives the probability to find a certain neighboring atom at a specific radial distance (R) to the absorbing atom. Thus, EXAFS can give us information about the nature of atoms bound to

a Cu center before, during and after the catalytic reaction. When bound to the tmpa ligand, the neighboring atoms to Cu are nitrogen, while in the case of Cu cluster formation a Cu-Cu contribution may be found in EXAFS.

Cu-tmpaCOOH (tmpa = tris(2-pyridylmethyl)amine) was synthesized and incorporated into the NU1000 MOF by solvent-assisted ligand incorporation (SALI) as described in Chapter 2 to form NU1000|Cu-tmpaCOOH.[41] All measurements described in this chapter were performed using a MOF with a loading of 0.8 Cu centers per Zr node. Cyclic voltammetry (CV) of this MOF under Ar atmosphere shows a redox wave at 0.24 V vs. RHE (Figure 2.6 and Figure 3.1) that is assigned to the $Cu^{II/I}$ redox couple. CV under O_2 atmosphere shows a catalytic current with an onset potential of 0.33 V vs. RHE and a current density of −40 mA cm^{-2} and with chronoamperometry (CA) at 0.3 V vs. RHE a catalytic current density is reached of −7.5 mA cm^{-2} (Figure 2.7). After electrolysis, a new irreversible redox couple is observed at 0.52 V vs. RHE in the CV under Ar (Figure 2.8a and Figure 3.1), indicating formation of a new species.

A very similar irreversible redox couple at 0.45 V vs. RHE was reported by Hupp and coworkers for Cu nanoparticles installed in NU1000.[43] In their work, Cu^{2+} ions were incorporated solvothermally, and nanoparticles were formed by CA at −0.57 V vs. RHE for 20 minutes. The nanoparticles were identified using transmission electron microscopy (TEM) and reached a diameter of ca. 5 nm. The redox couple associated with the nanoparticles is similar to what we find after catalysis for NU1000|Cu-tmpaCOOH.

Operando XAS was applied to uncover what species are formed during CA in NU1000|Cu-tmpaCOOH. Unlike microscopic methods, operando XAS can (1) confirm whether very small (< 5 nm) Cu particles are indeed formed under electrocatalytic conditions, (2) identify the nature of their potential-dependent character, and (3) determine which structure corresponds to the redox couple formed during electrocatalysis. The MOF was dispersed in an ink containing carbon black, Nafion, and acetone as previously reported.[41] The as-prepared ink was drop casted onto a carbon paper working electrode and used for operando XAS measurements in fluorescence mode. An electrochemical cell (Figure 3.1 and Figure B1) with a Kapton window was used with a constant flow of O_2 or He saturated 0.1 M phosphate buffer pH 7.

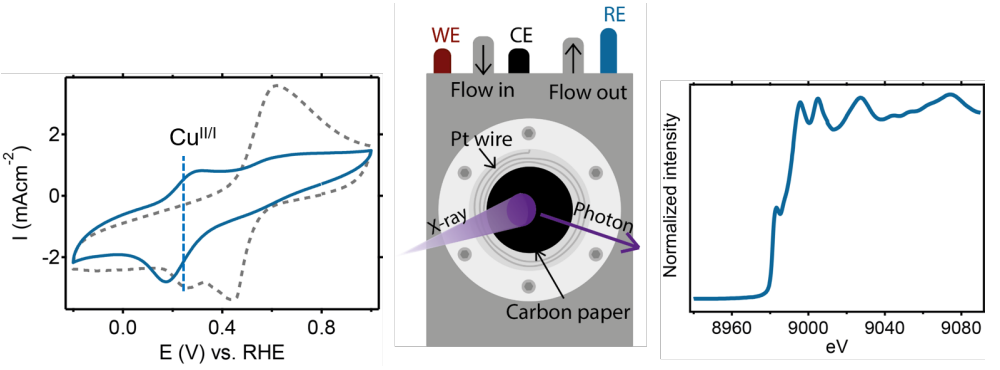

Figure 3.1 Schematic presentation of the operando X-ray absorption spectroscopy experiment. CV of NU1000|Cu-tmpaCOOH under Ar atmosphere before electrolysis (left panel, blue line) and after 6h electrolysis at 0.3 V vs. RHE under O_2 atmosphere (left panel, grey dashed line), schematic presentation of the operando experiment (middle) and resulting Cu K-edge XANES spectrum (right panel).

3.2.2 X-ray absorption near-edge spectroscopy

X-ray absorption near-edge spectroscopy (XANES) of as-prepared NU1000|Cu-tmpaCOOH yields two pre-edge features at 8977 and 8982 eV, which qualitatively coincide with the pre-edge features of $Cu(OH)_2$ and Cu_2O, respectively (Figure 3.2 and Figure B2). However, the linear combination fitting (LCF) of the sample using those two references does not yield a good fit (Figure 3.3a). The addition of Cu^0 foil as a reference does not improve the quality of the fit (Figure 3.3b). Qualitatively, NU1000|Cu-tmpaCOOH closely resembles the XANES spectrum of $Cu(OH)_2$ with possibly a small Cu^0 contribution (Figure 3.3c). This strongly implies a Cu^{2+} dominant character of the Cu sites in the catalyst. Once placed inside the electrochemical XAS cell and exposed to the O_2-saturated electrolyte at open circuit potential (OCP), we do not observe any noticeable change in the XANES features (Figure B3). This suggests that the chemical state of the Cu sites existing in the as-prepared catalyst remains stable at OCP. A succession of XANES scans measured for 40 minutes does not indicate any time-dependent change (Figure B4). This suggests that beam-induced damage is negligible if present at all.

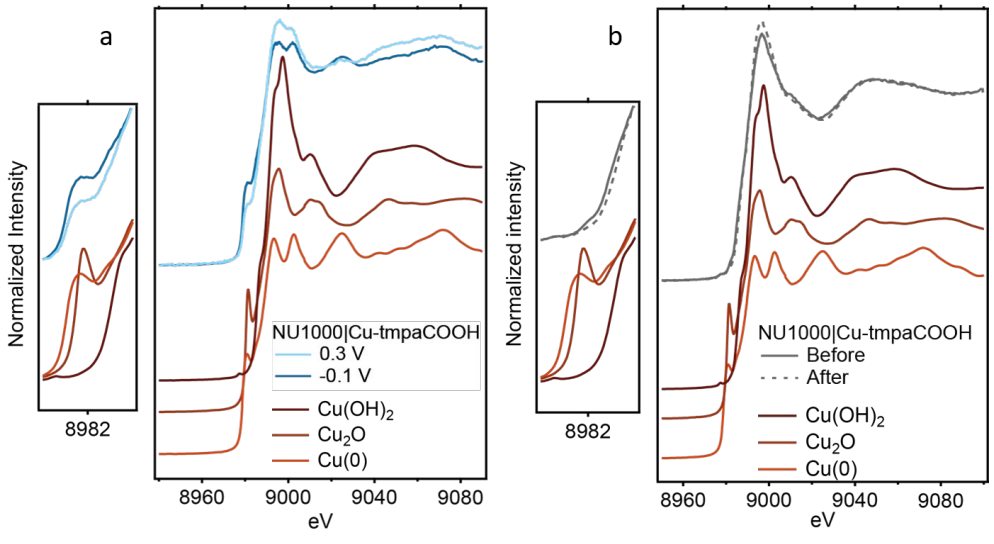

Figure 3.2 XANES of NU1000|Cu-tmpaCOOH during CA under O_2 atmosphere at 0.3 V vs. RHE (a, light blue), at −0.1 V vs. RHE (a, dark blue), before CA (b, grey) and after CA (b, grey dashed) including zoom of the pre-edge region. XANES of Cu foil, Cu_2O and $Cu(OH)_2$ standards are given in red.

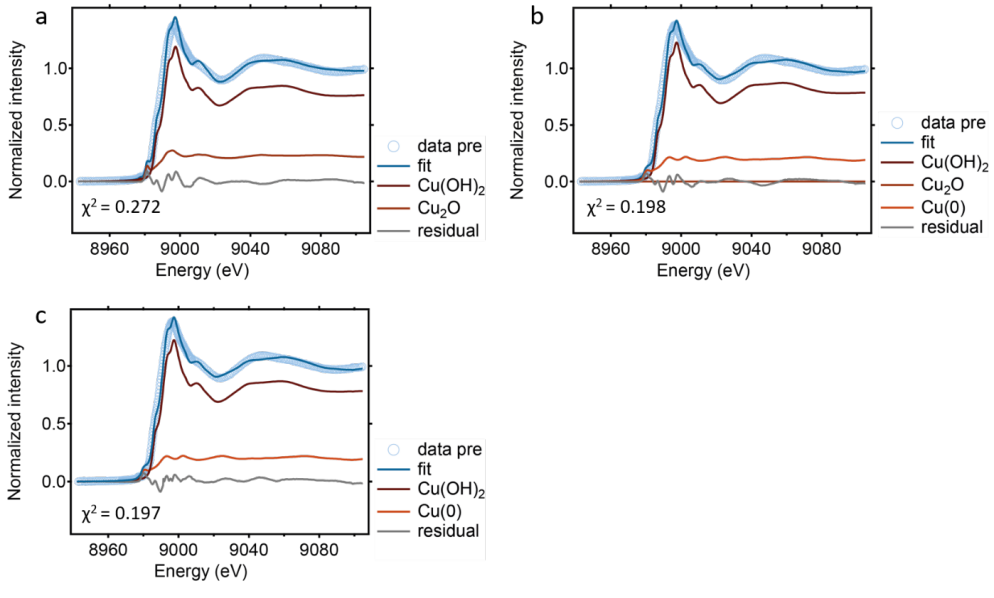

Figure 3.3 Linear combination fitting (LCF) of the Cu K-edge XANES spectrum of NU1000|Cu-tmpaCOOH at OCP with $Cu(OH)_2$ and Cu_2O (a), with $Cu(OH)_2$, Cu_2O and Cu(0) (b), and with $Cu(OH)_2$ and Cu(0) (c).

Once the absence of beam-induced change was confirmed, a more negative potential of 0.3 V vs. RHE was applied (Figure B7). We already observe formation of Cu^0 species 30 mV negative of the onset potential at 0.33 V vs RHE (Figure 3.2a). Similar to the sample before electrolysis, LCF using Cu^0 foil and $Cu(OH)_2$ yields better fits than LCF including Cu_2O (Figure 3.4). An LCF using Cu^0 foil and $Cu(OH)_2$ indicates a 50:50 Cu^0:Cu^{2+} ratio (Figure 3.4a, Table B1). At a more negative potential of –0.1 V vs. RHE, an even greater Cu^0 fraction of 78% is measured (Figure 3.4c, Table B1). After returning to OCP, the post-electrolysis spectrum is nearly identical to the pre-electrolysis one (Figure 3.2b). Similarly to before electrolysis, the Cu species in the MOF exhibit a Cu^{2+} dominating oxidation state, as evidenced by the pre-edge still observed at 8977 eV. However, the pre-edge feature previously observed at 8982 eV is no longer visible. This suggests that although the dominant Cu state is mostly unchanged, a structural rearrangement has occurred during ORR.

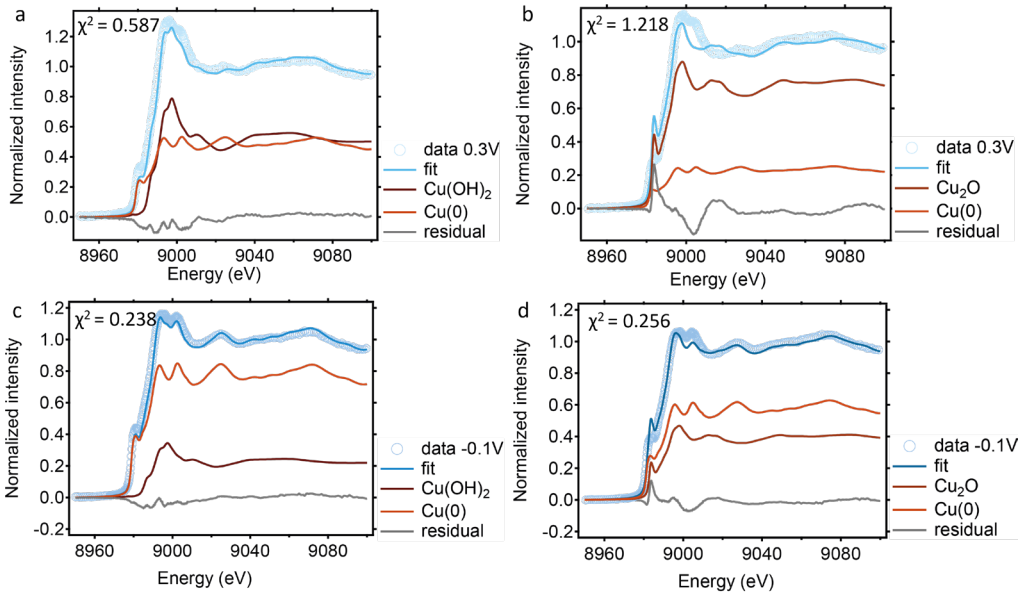

Figure 3.4 Linear combination fitting (LCF) of the Cu K-edge XANES spectrum of NU1000|Cu-tmpaCOOH in O_2 saturated phosphate buffer pH 7 at −0.1 V vs. RHE with (a) $Cu(OH)_2$ and Cu^0 and (b) Cu_2O and Cu^0 and at 0.3 V vs. RHE with (c) $Cu(OH)_2$ and Cu^0 and (d) Cu_2O and Cu^0. The resulting fractions of Cu oxidation states are reported in Table B1.

Multivariate curve resolution (MCR) analysis was applied to better understand the chemical transformation of our system and verify the observations using LCF analysis (Figure B5). According to the imperfect fitting observed with LCF and given the complexity of matching

the coordination environment of the Cu complex, it is not surprising that LCF is insufficient to represent the mixture of phases changing as a function of the applied potential. We assume that three main components must define the state of the molecular catalyst in the MOF (Figure B6). MCR analysis identifies two components that are indeed nearly identical to the XAS features from Cu^0 of Cu foil and Cu^{2+} of $Cu(OH)_2$ (Figure 3.5 and Figure B5). The third component exhibits a main edge at 8980 eV, which is situated between edges of a Cu^+ and a Cu^{2+} state. However, its absorption features are very dissimilar to any common standards. This unknown third component may be attributed to the MOF-embedded Cu(II)-tmpaCOOH molecular catalyst still partially coordinated to a triflate anion (OTf^-) used in its synthesis, or to a H_2O molecule. Monitored as a function of the applied potential and time, the oxidation state of the Cu molecular catalyst is progressively reduced at −0.1 V to a Cu^0 phase after 2 hours of CA (Figure 3.5b). When returned to OCP after the CA measurement, the 3rd MCR component initially present (ca. 35%) is no longer observed. Only the Cu^{2+} phase present at the start (ca. 75%) is recovered at OCP and represents nearly the sole phase in the system. Such a change corroborates the hypothesis that the molecular catalyst undergoes an irreversible structural transformation after being subjected to electrocatalytic reaction conditions.

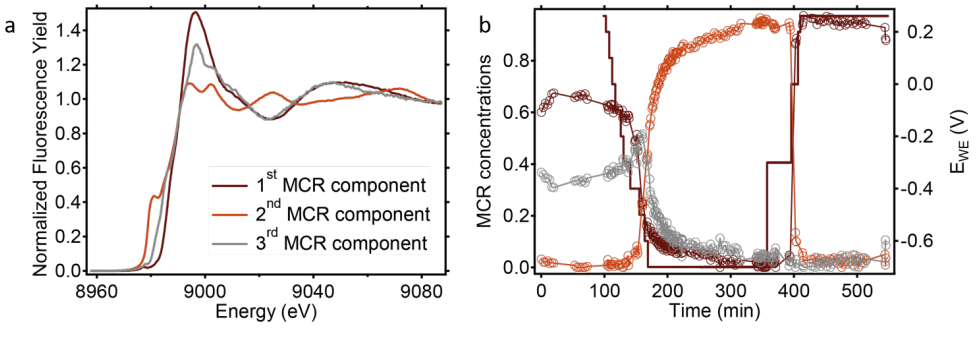

Figure 3.5 MCR fitting of NU1000|Cu-tmpaCOOH at −0.1 V vs. RHE under O_2 atmosphere yields three distinct components (a). The relative ratio of the three MCR fitting components as a function of time and the applied potential (b) indicates the progressive change in the distribution of Cu states in the sample. A complete loss of the 3rd MCR component is observed after carrying out electrolysis at −0.1 V vs. RHE for ca. 3 hours.

3.2.3 Extended X-ray absorption fine structure

The Cu K-edge extended X-ray absorption fine structure (EXAFS) was evaluated to gain further understanding of structural changes of the system and the radial distance plots (R-space) are shown in Figure 3.6. Regardless of the exact atomic structure of the Cu sites, one

can qualitatively evaluate the EXAFS signal in the R-space to distinguish the presence of Cu bonds with lighter elements (e.g., O, N, or S) between 1 and 2 Å, or with other metal atoms (e.g., Cu, Zr, Ni or Fe) between 2 and 3 Å. Peaks in the 2-3 Å range can principally be attributed to a Cu-Cu scattering path. However, because of the presence of Zr in the MOF itself, contribution of Cu-Zr paths to the Cu K-edge EXAFS cannot be completely ruled out. As Cu-Cu and Cu-Zr signals are expected to show below and above 2.6 Å, respectively,[44] in-depth analysis of the EXAFS fitting could help better assess their relative contribution if they coexist in the sample.

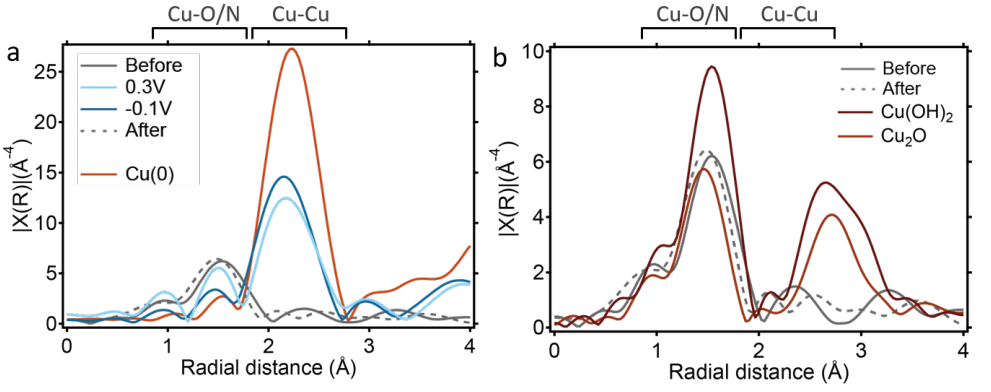

Figure 3.6 EXAFS of NU1000|Cu-tmpaCOOH before (b, grey), after (b, grey dashed) and during CA at 0.3 V vs. RHE (a, light blue) and −0.1 V vs. RHE (a, dark blue). EXAFS of Cu standards are shown in red.

Before the reaction, EXAFS of the NU1000|Cu-tmpaCOOH features a peak where Cu-O or Cu-N scattering paths are expected. As soon as a potential is applied, a peak at 2.23 Å is observed. Fitting of the first shell of Cu-Cu yields a coordination number $N_{Cu\text{-}Cu}$ of 8.35 ± 1.54 positioned at a radial distance of 2.55 ± 0.01 Å (Figure 3.7a and Table 3.1). These values are consistent with the hypothesis of Cu^0 clusters forming during electrolysis. The data was fitted for 3<k<11.6 and 1.6<R<3, using solely the first Cu-Cu scattering path calculated by the FEFF model of fcc Cu^0. The negligible amount of oxide phases highlighted by the MCR analysis indicates it is unnecessary to include them in the model used for data fitting. According to the model of Jentys for small, face-centered cubic (fcc) metallic particles,[45] and assuming a homogeneous distribution of formed particles, this coordination number corresponds to 1.8 nm diameter clusters (Figure 3.7b). As also suggested by XANES, formation of these Cu^0 clusters appears to be more pronounced at more negative applied potentials with a corresponding decrease of the Cu-O/N peak intensity and simultaneous increase of the Cu-Cu peak (Figure 3.6a).

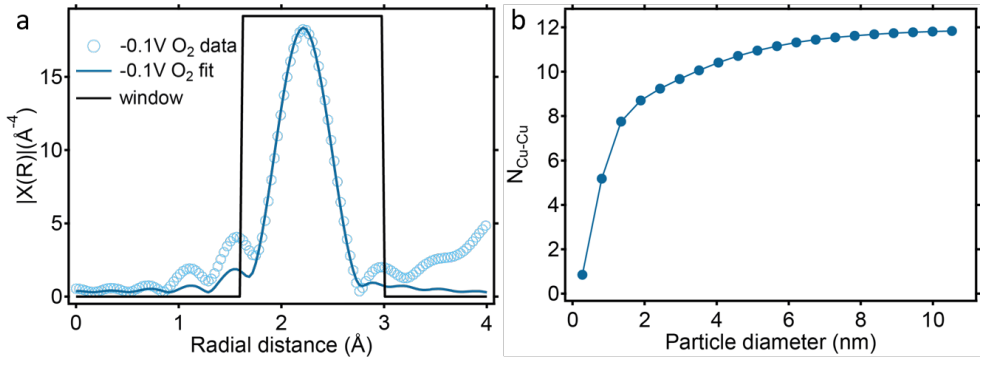

Figure 3.7 First shell fit of the Cu K-edge EXAFS of NU1000|CutmpaCOOH in O_2 saturated phosphate buffer pH 7 at −0.1 V vs. RHE. The EXAFS-derived parameters summarized in Table 3.1 (a) and coordination number N_{Cu-Cu} dependence on the particle diameter as described by Jentys for a cuboctahedral shape (b).[45] N_{Cu-Cu} of 8.35 corresponds to a particle diameter of ca. 1.8 nm.

Table 3.1 EXAFS fitting parameters for the fit displayed in Figure 3.7.

	N	ΔR (Å)	σ^2
Cu-Cu	8.35 (±1.54)	2.55 (±0.01)	0.008 (±0.002)
ΔE_{Cu}	−2.54 (±1.87)		
Reduced χ^2	91.88		
R-factor	0.015		

The peak observed at 1.5 Å before the reaction is recovered post-electrolysis. Qualitatively, the peak distribution of the sample EXAFS differs from the EXAFS of both Cu_2O and $Cu(OH)_2$ standards. This is consistent with the poor LCF using these references as fitting standards. In addition, the Cu species in NU1000|Cu-tmpaCOOH before and after electrocatalysis exhibit a slight shift of the first scattering peak to smaller radial distances (Figure 3.6b). This could suggest either a change in the distribution of oxidation states or a contraction of the original Cu structure upon exposure to electrocatalytic conditions. Such an observation remains consistent with the hypothesis of cluster formation.

Formed under reductive conditions, unprotected Cu^0 clusters are prone to oxidation once returned to more oxidative conditions. In their work on Cu single atom catalysts on N-doped carbon, Fontecave and coworkers proposed that the presence of Cu^{2+} before and after electrolysis, and of Cu^0 observed using in-situ XANES are the result of reversible formation of Cu^0 clusters.[39] However, no electrochemical characterization was presented to confirm that the Cu species before and after electrolysis are identical. In this chapter, it can be

confidently claimed that the Cu species after electrolysis differ from the original species, as illustrated by the vastly different redox couples identified electrochemically. This surface-sensitive characterization method identifies two different active surface species, which correspond, for a bulk-sensitive technique like EXAFS, to moderately different signals. However, careful MCR analysis of the XAS signal throughout the life cycle of the catalyst helps corroborate the differences identified electrochemically; the 3rd component representative of the molecular Cu catalyst's initial state completely disappears post-electrolysis.

3.2.4 XANES and EXAFS combined

Overall, the XANES and EXAFS results are consistent with the formation of Cu^0 clusters during CA at 0.3 V and −0.1 V vs. RHE. The hypotheses about the state of the Cu catalyst before, during and after the catalytic reaction, information that can be extracted from the XAS measurements, are summarized in Figure 3.8. Before the experiment, the sample exhibits a Cu^{2+} character with no observable Cu-Cu distances, consistent with the presence of the Cu-tmpaCOOH catalyst. This species remains intact at OCP. When a potential of ≤ 0.3 V vs. RHE is applied, Cu^0 clusters are formed (Figure 3.8). It is likely that the Cu-tmpaCOOH catalyst first reduces to its Cu^+ state and is then further reduced to Cu^0 clusters. It is well known that non-coordinated Cu^+ species easily disproportionate to form Cu^0 and Cu^{2+}.[46]

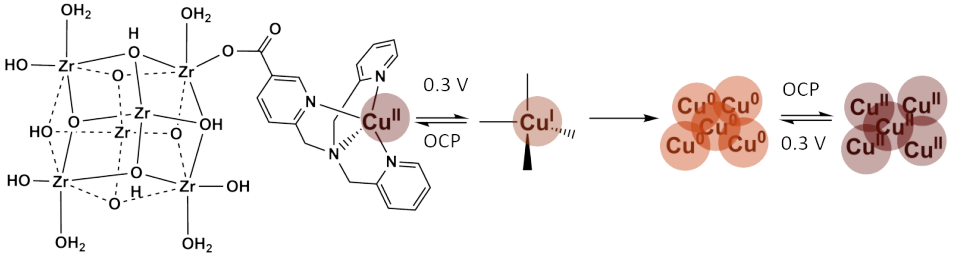

Figure 3.8 Schematic representation of the Cu-species hypothesized to be formed before, during and after ORR by NU1000|Cu-tmpaCOOH.

XANES and EXAFS spectra of NU1000|Cu-tmpaCOOH measured every 10 minutes for the first 40 minutes of CA at 0.3 V vs. RHE under O_2 atmosphere (Figure 3.9) show that Cu clusters are formed over time at this potential. XANES and EXAFS spectra of NU1000|Cu-tmpaCOOH measured during CA at –0.1 V vs. RHE under He atmosphere (Figure 3.10) show that formation of Cu^0 clusters is not dependent on the presence of O_2. Therefore, the formation of Cu^0 clusters is assumed to be caused only by application of a reductive potential. These clusters then oxidize to Cu^{2+} after returning to OCP, i.e., when an active

bias is no longer applied. The Cu^{2+} state of these now oxidized clusters differs from the initial Cu^{2+} state of the Cu(II)-tmpaCOOH molecular catalyst identified by CV and MCR analysis. According to the latter, only one out of the two Cu^{2+} components observed before electrolysis remains after the reaction. We propose that the formed Cu^{2+} compound has a coordination environment akin to $Cu(OH)_2$ (Figure B5) and is responsible for the new redox couple observed electrochemically after catalysis. These clusters are likely a type of CuOx species as a reported EXAFS for atomically dispersed CuOx species shows similarity to ours.[47] However, in the Cu^{2+} oxidation state it is difficult to distinguish between clusters and molecular species by EXAFS alone and a technique such as high resolution transmission electron microscopy should be employed to obtain more certainty. Given the good reusability of the NU1000|Cu-tmpaCOOH system,[41] oxidation of Cu^0 to Cu^{2+} clusters is expected to be reversible.

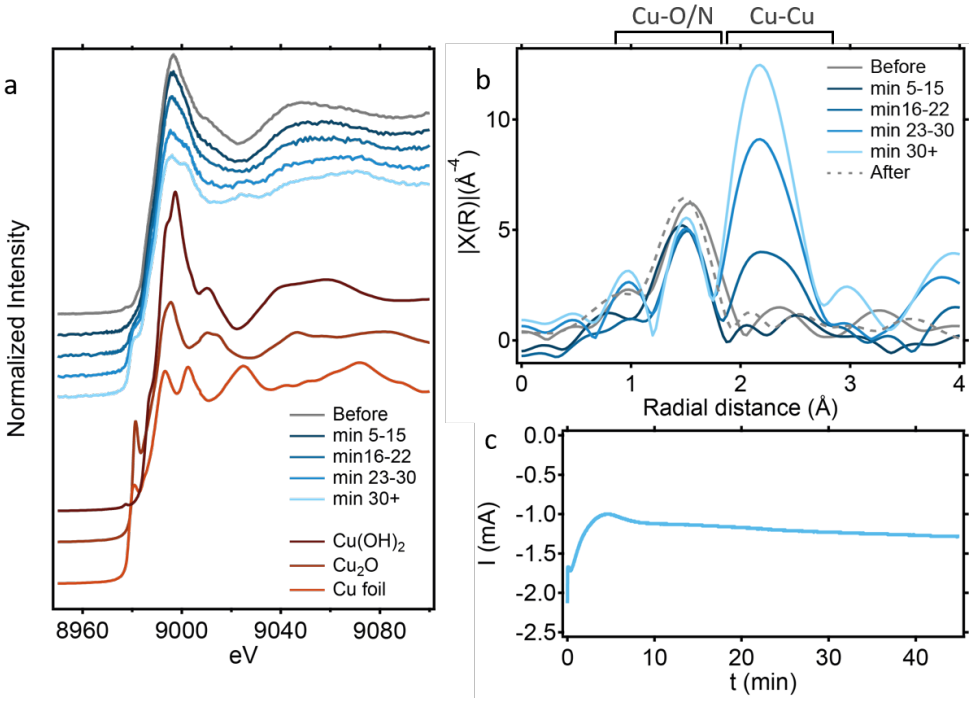

Figure 3.9 Cu K-edge XANES (a) and EXAFS (b) spectra of NU1000|Cu-tmpaCOOH measured every 10 minutes for the first 40 minutes of CA at 0.3V under O_2 atmosphere (c). The XANES spectra for Cu^0, Cu^+ and Cu^{2+} references are shown in red. Each scan takes 10 minutes and is measured directly after the previous one.

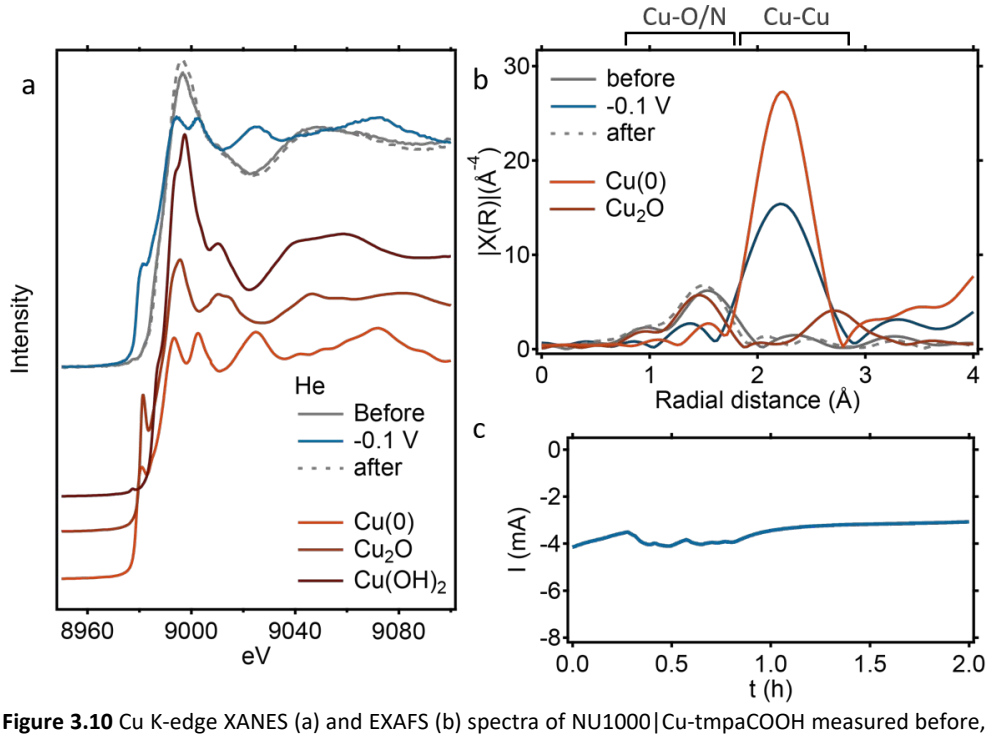

Figure 3.10 Cu K-edge XANES (a) and EXAFS (b) spectra of NU1000|Cu-tmpaCOOH measured before, during and after CA at −0.1V under He atmosphere (c). The XANES and EXAFS spectra for Cu^0, Cu^+ and Cu^{2+} references are shown in red.

There is an evident difference in behavior between Cu-tmpa in a homogeneous solution and when immobilized in a MOF. In a homogeneous solution, there is very little deposition of Cu^0 on the electrode, and the activity is driven by the Cu-tmpa catalyst in the Cu^+ oxidation state.[37,38] In the NU1000|Cu-tmpaCOOH MOF, formation of Cu^0 clusters is observed, that are deemed responsible for the measured ORR activity. A probable driver for the formation of clusters in MOFs is the high local concentration of Cu atoms that can direct the equilibrium between Cu-tmpa catalysts and Cu clusters toward the clusters. Evidently, the confinement effects achieved through embedding the catalyst in a MOF are accompanied by an unintended aggregation of the molecular Cu catalysts, thus resulting in loss of homogeneity. These findings illustrate the necessity of employing operando spectroscopy to monitor the dynamics, and thus, the true active state of molecular catalysts in MOFs.

3.3 Conclusion

In this chapter, the Cu species formed in the NU1000|Cu-tmpaCOOH MOF before, during, and after the ORR were studied using XAS. The catalyst, with an initial Cu^{2+} oxidation state, forms Cu^0 clusters upon application of a potential of 0.3 V vs. RHE. The extent of cluster formation increases with more negative potential. After the reaction, the Cu sites reoxidize to a Cu^{2+} oxidation state with a coordination sphere resembling that of heterogeneous $Cu(OH)_2$. This work illustrates the dynamic nature of Cu-based molecular catalysts in MOFs and highlights the importance of operando investigation of the species formed during electrocatalysis. This work shows that even though electrocatalytic performance can improve by embedding a molecular catalyst in a MOF, it cannot be assumed these catalysts stay molecular, even if the homogeneous parent systems do. As illustrated in parallel works, this knowledge seems to be especially important for Cu-based catalysts whose dynamic behavior drives their reconstruction regardless of the hosting support. Such aspects exemplify the necessity of not only applying operando spectroscopy techniques to the study of molecular catalysts embedded in MOFs, but also of carefully comparing those characterization results to electrochemical results. In that way, the chemical nature of the bulk and of the surface of the studied catalytic system can be distinguished.

3.4 Experimental

3.4.1 Materials

Chemicals were purchased from commercial suppliers and used without further purification. Milli-Q Ultrapure grade water (>18.2 MΩ cm resistivity) was used for all electrochemical experiments and for the preparation of electrolyte. H23I2 carbon paper with microporous layer was purchased from FuelCellStore.

3.4.2 Sample preparation for operando XAS spectroscopy

An ink was prepared by adding 2 mg MOF, 1 mg carbon black, 20 µL Nafion© perfluorinated resin solution in propanol and 180 µL acetone to a vial and vortexing, followed by 15 minutes ultrasonication and vortexing once more. The MOF ink was drop casted onto the carbon paper working electrode and allowed to dry for 1 hour before use. O_2 or He saturated 0.1M phosphate buffer pH 7 was flowed through the cell at a flow rate of 1.4 mL/min.

3.4.3 X-ray absorption spectroscopy

X-ray absorption spectroscopy (XAS) experiments were conducted at the ALBA synchrotron at beamline BL 22 CLAESS. All ex-situ samples were characterized in transmission mode while all the in-situ measurements were carried out in fluorescence mode using RaySpec silicon drift detector equipped with 6 Be windows. The XANES and EXAFS data processing, including energy calibration and edge step normalization, was done in Athena. The linear combination fitting (LCF) was also carried out in the same software. EXAFS fitting was performed in Artemis according to previous procedures.[48] Both programs are part of Demeter package 0.9.26.[49] Two FEFF models of Cu^0 and CuO were generated for the EXAFS fitting. Only the first single scattering path to the first shell from Cu^0 and the first O single scattering path in CuO were used for the fit.

The evolution of Cu phases measured with XANES was also evaluated by applying the principal component analysis (PCA) approach implemented in PyFitit code.[50] Spectra were calibrated, normalized, and then treated as a single dataset. The minimum number of pure components was set to 3 using Scree Plot approach (Figure B6). A minimum number of pure components was used in the simplisma procedure to obtain an initial estimation for the spectra of the pure components directly from the data set.[51] Then MCR-ALS algorithm was applied with non-negativity for spectra and concentration profiles,[52] and the sum of MCR concentrations was constrained to 1.

For operando measurements, a commercial Zahner PECC-2 3-electrodes flow cell was used (Figure B1). The front window (facing the X-ray and the detector) was made of Al and the back window made of Teflon. An Al contact cover was pressed against the carbon paper working electrode to establish the working electrode connection. The working electrode was a carbon paper with gas diffusion electrode cut into a circle with a ±3 cm diameter. The counter electrode was a Pt wire coiled against the back window of the cell. A leakless miniature Ag/AgCl (ET072-1) was used as the reference electrode. The electrolyte was flown through the electrode using a peristaltic D-25Vplus pump (Dinko Instruments). The used electrolyte was purged and saturated with either 21% O_2 + He or He only, before being introduced into the cell. All electrodes were connected to a VSP potentiostat (Biologic) and the electrochemical programs controlled using EC-Lab.

The electrochemical cell was bolted to a stage which was controlled remotely. Before each XAS measurement, the cell position was aligned to (1) ensure the measured spot was within

a homogeneous sample distribution position and (2) optimize the XAS signal intensity. The beam size was optimized to ensure enough Cu signal was detected while minimizing beam exposure on the sample. Overall, the beam spot size used was set to 0.5 × 0.8 mm (V × H) and the photon flux about 10^{13} photons/s. When not measuring, the beam was turned off to minimize risk of beam damage.

3.5 References

[1] R. F. Heck, *Organic Reactions* **1982**, 345–390.

[2] N. Miyaura, K. Yamada, A. Suzuki, *Tetrahedron Lett* **1979**, *20*, 3437–3440.

[3] A. O. King, N. Okukado, E. I. Negishi, *J Chem Soc Chem Commun* **1977**, 683–684.

[4] R. H. Grubbs, T. M. Trnka, in *Ruthenium in Organic Synthesis*, John Wiley & Sons, Ltd, **2004**, pp. 153–177.

[5] W. S. Knowles, *Acc Chem Res* **1983**, *16*, 106–112.

[6] R. H. Crabtree, *Chem Rev* **2015**, *115*, 127–150.

[7] R. H. Crabtree, *Chem Rev* **2012**, *112*, 1536–1554.

[8] P. Pelosin, M. Gil-Sepulcre, P. Garrido-Barros, D. Moonshiram, J. Benet-Buchholz, C. Gimbert-Suriñach, A. Llobet, *iScience* **2020**, *23*, 101378.

[9] D. B. Grotjahn, D. B. Brown, J. K. Martin, D. C. Marelius, M. C. Abadjian, H. N. Tran, G. Kalyuzhny, K. S. Vecchio, Z. G. Specht, S. A. Cortes-Llamas, V. Miranda-Soto, C. Van Niekerk, C. E. Moore, A. L. Rheingold, *J Am Chem Soc* **2011**, *133*, 19024–19027.

[10] J. J. Stracke, R. G. Finke, *J Am Chem Soc* **2011**, *133*, 14872–14875.

[11] B. Van Dijk, J. P. Hofmann, D. G. H. Hetterscheid, *Physical Chemistry Chemical Physics* **2018**, *20*, 19625–19634.

[12] Z. Weng, Y. Wu, M. Wang, J. Jiang, K. Yang, S. Huo, X. F. Wang, Q. Ma, G. W. Brudvig, V. S. Batista, Y. Liang, Z. Feng, H. Wang, *Nat Commun* **2018**, *9*, 1–9.

[13] D. G. H. Hetterscheid, *Chemical Communications* **2017**, *53*, 10622–10631.

[14] K. Köhnke, N. Wessel, J. Esteban, J. Jin, A. J. Vorholt, W. Leitner, *Green Chemistry* **2022**, *24*, 1951–1972.

[15] D. G. H. Hetterscheid, C. J. M. Van Der Ham, O. Diaz-Morales, M. W. G. M. Verhoeven, A. Longo, D. Banerjee, J. W. Niemantsverdriet, J. N. H. Reek, M. C. Feiters, *Physical Chemistry Chemical Physics* **2016**, *18*, 10931–10940.

[16] T. E. Rosser, E. Reisner, *ACS Catal* **2017**, *7*, 3131–3141.

[17] H. Baltruschat, *J Am Soc Mass Spectrom* **2004**, *15*, 1693–1706.

[18] T. Senthamarai, K. Murugesan, J. Schneidewind, N. V. Kalevaru, W. Baumann, H. Neumann, P. C. J. Kamer, M. Beller, R. V. Jagadeesh, *Nat Commun* **2018**, *9*, 1–12.

[19] S. N. Macmillan, K. M. Lancaster, *ACS Catal* **2017**, *7*, 1776–1791.

[20] S. Mukhopadhyay, O. Basu, A. Kar, S. K. Das, *Inorg Chem* **2020**, *59*, 472–483.

[21] S. Roy, Z. Huang, A. Bhunia, A. Castner, A. K. Gupta, X. Zou, S. Ott, *J Am Chem Soc* **2019**, *141*, 15942–15950.

[22] K. Hemmer, M. Cokoja, R. A. Fischer, *ChemCatChem* **2021**, *13*, 1683–1691.

[23] V. Mouarrawis, R. Plessius, J. I. van der Vlugt, J. N. H. Reek, *Front Chem* **2018**, *6*, 623.

[24] Y. Wang, H. Cui, Z. W. Wei, H. P. Wang, L. Zhang, C. Y. Su, *Chem Sci* **2016**, *8*, 775–780.

[25] W. Zheng, L. Y. S. Lee, *ACS Energy Lett* **2021**, *6*, 2838–2843.

[26] S. Iniyan, J. Ren, S. Deshmukh, K. Rajeswaran, G. Jegan, H. Hou, V. Suryanarayanan, V. Murugadoss, M. Kathiresan, Ben, B. Xu, Z. Guo, *The Chemical Record* **2023**, *23*, e202300317.

[27] N. F. Suremann, B. D. McCarthy, W. Gschwind, A. Kumar, B. A. Johnson, L. Hammarström, S. Ott, *Chem Rev* **2023**, *123*, 6545–6611.

[28] Y. Peng, S. Sanati, A. Morsali, H. García, S. Sanati, P. Hermenegildo García, P. A. Morsali, *Angewandte Chemie International Edition* **2022**, *62*, e202214707.

[29] S. Hindocha, *The Chemistry of Metal-Organic Frameworks: Synthesis, Characterization, and Applications*, **2017**.

[30] J. Reedijk, *Platin Met Rev* **2008**, *52*, 2–11.

[31] N. Sakamoto, K. Sekizawa, S. Shirai, T. Nonaka, T. Arai, S. Sato, T. Morikawa, *Nat Catal* **2024**, *7*, 574–584.

[32] B. Yang, L. Chen, S. Xue, H. Sun, K. Feng, Y. Chen, X. Zhang, L. Xiao, Y. Qin, J. Zhong, Z. Deng, Y. Jiao, Y. Peng, *Nat Commun* **2022**, *13*, 1–13.

[33] P. Zhang, M. Wang, Y. Yang, T. Yao, L. Sun, *Angewandte Chemie International Edition* **2014**, *53*, 13803–13807.

[34] H. Lei, H. Fang, Y. Han, W. Lai, X. Fu, R. Cao, *ACS Catal* **2015**, *5*, 5145–5153.

[35] Q. F. Chen, Z. Y. Cheng, R. Z. Liao, M. T. Zhang, *J Am Chem Soc* **2021**, *143*, 19761–19768.

[36] D. den Boer, H. Stegman, C. J. C. Peeters, M. A. Siegler, D. G. H. Hetterscheid, *Eur J Inorg Chem* **2024**, *27*, e202300475.

[37] M. Langerman, D. G. H. Hetterscheid, *Angewandte Chemie International Edition* **2019**, *58*, 12974–12978.

[38] P. H. van Langevelde, D. G. H. Hetterscheid, *Chem Catalysis* **2024**, *4*, 101069.

[39] D. Karapinar, N. T. Huan, N. Ranjbar Sahraie, J. Li, D. Wakerley, N. Touati, S. Zanna, D. Taverna, L. H. Galvão Tizei, A. Zitolo, F. Jaouen, V. Mougel, M. Fontecave, *Angewandte Chemie International Edition* **2019**, *58*, 15098–15103.

[40] C. E. Creissen, M. Fontecave, *Nat Commun* **2022**, *13*, 1–4.

[41] M. E. Hoefnagel, D. Rademaker, D. G. H. Hetterscheid, *ChemSusChem* **2023**, *16*, e202300392.

[42] J. Timoshenko, B. Roldan Cuenya, *Chem Rev* **2021**, *121*, 882–961.

[43] C. W. Kung, C. O. Audu, A. W. Peters, H. Noh, O. K. Farha, J. T. Hupp, *ACS Energy Lett* **2017**, *2*, 2394–2401.

[44] J. Antonowicz, A. Pietnoczka, W. Zalewski, R. Bacewicz, M. Stoica, K. Georgarakis, A. R. Yavari, *J Alloys Compd* **2011**, *509*, S34–S37.

[45] A. Jentys, *Physical Chemistry Chemical Physics* **1999**, *1*, 4059–4063.

[46] C. S. Day, R. Martin, *Chem Soc Rev* **2023**, *52*, 6601–6616.

[47] A. Liu, L. Liu, Y. Cao, J. Wang, R. Si, F. Gao, L. Dong, *ACS Catal* **2019**, *9*, 9840–9851.

[48] D. Kim, N. Becknell, Y. Yu, P. Yang, *Nano Lett* **2017**, *17*, 2732–2737.

[49] B. Ravel, M. Newville, *J. Synchrotron Rad.* **2005**, *12*, 537–541.

[50] A. Martini, S. A. Guda, A. A. Guda, G. Smolentsev, A. Algasov, O. Usoltsev, M. A. Soldatov, A. Bugaev, Y. Rusalev, C. Lamberti, A. V. Soldatov, *Comput Phys Commun* **2020**, *250*, 107064.

[51] W. Windig, J. Guilment, *Anal Chem* **1991**, *63*, 1425–1432.

[52] S. Hugelier, R. Vitale, C. Ruckebusch, *Appl Spectrosc* **2018**, *72*, 420–431.